


Cite this: *RSC Adv.*, 2019, 9, 10865Received 10th January 2019  
Accepted 31st March 2019

DOI: 10.1039/c9ra00206e

rsc.li/rsc-advances

# From metal–organic framework to morphology- and size-controlled 3D mesoporous Cr<sub>2</sub>O<sub>3</sub> toward a high surface area and enhanced volatile organic compound oxidation catalyst†

Xiutao Li,  Qichen Zhao, Junyu Qiao, Qingsong Zhang and Xiaomeng Zhou\*

Morphology- and size-controlled 3D mesoporous Cr<sub>2</sub>O<sub>3</sub> have always been a research hotspot due to their wide applications. Herein, we for the first time report that the carbonized Cr-MOFs can ignite spontaneously at room temperature and form the corresponding 3D mesoporous Cr<sub>2</sub>O<sub>3</sub> with high specific surface areas (219.25 to 303.44 cm<sup>2</sup> g<sup>−1</sup>). More importantly, the shape and size of 3D mesoporous Cr<sub>2</sub>O<sub>3</sub> can be well controlled by a facile adjustment of the Cr-MOF synthesis conditions. Furthermore, these materials showed an exceptionally high catalytic performance in formaldehyde oxidation. These results are predicted to offer a novel method in the design and synthesis of 3D porous Cr<sub>2</sub>O<sub>3</sub>.

## Introduction

Chromium oxide (Cr<sub>2</sub>O<sub>3</sub>) has been extensively investigated due to its possible industrial applications in catalysis, lithium ion batteries, magnetics, gas sensors, wear resistance, H<sub>2</sub> absorption material and so on.<sup>1–11</sup> Up to now, various distinct structures of Cr<sub>2</sub>O<sub>3</sub> have been reported, such as nanofibers,<sup>1,2</sup> hollow microspheres,<sup>3,4</sup> hollow hexagonal pellets<sup>5</sup> and three-dimensional (3D) mesoporous structures.<sup>6–12</sup> Among these morphological structures, 3D porous architectures have attracted increasing attention in recent years, due to their high surface-to-volume ratio and permeability. In the past, large amounts of effort have been focused on surfactant-templating methods with solid porous silica or carbon (*e.g.* KIT-6, SBA-15, MCM-41 and PMMA) to synthesize ordered porous structures, however, template-assisted processes have shortcomings for practical applications owing to the high cost, low yield and environmental concerns. Moreover, it is difficult to fabricate 3D porous Cr<sub>2</sub>O<sub>3</sub> with controlled shape and size. The design and synthesis of metal oxides with different sizes and shapes have stimulated great research interest, since the chemical and physical properties of the materials depend not only on their composition but also on their structures, sizes and morphologies.<sup>13–18</sup> Furthermore, it is well known that high surface area of materials could improve their surface performances, but there are rare 3D porous Cr<sub>2</sub>O<sub>3</sub> reported in previous works with specific surface area larger than 200 m<sup>2</sup> g<sup>−1</sup> (most of them near

100 m<sup>2</sup> g<sup>−1</sup>), which greatly limits the performance and applications of the porous Cr<sub>2</sub>O<sub>3</sub>. Thus, methods to synthesize 3D porous Cr<sub>2</sub>O<sub>3</sub> with high specific surface area, shape control, high yields, low cost and good reproducibility are desirable.

Recently, metal–organic frameworks (MOFs) derived porous metal oxides (Fe<sub>2</sub>O<sub>3</sub>,<sup>19</sup> Co<sub>3</sub>O<sub>4</sub>,<sup>20</sup> CuO,<sup>21</sup> NiO/ZnO<sup>22</sup>) by calcination in air have been reported. Due to the homogeneous distributions of the metal ions/clusters and highly porous structures in MOFs, the porous metal oxides with controlled shape and size and high surface areas can be well prepared by using proper annealing treatment. Although Voskanyan *et al.* have introduced a porous Cr<sub>2</sub>O<sub>3</sub> octahedra synthesis method using MIL-101(Cr) as a sacrificial template, the extra oxidizer and reducing agent are needed to initiate combustion reaction.<sup>23</sup>

Herein, we report a novel and facile route to synthesize 3D mesoporous Cr<sub>2</sub>O<sub>3</sub> with bipyramidal hexagonal prismatic and octahedral morphology and high surface area *via* a MOF auto-combustion method. Moreover, the morphology and size of 3D porous Cr<sub>2</sub>O<sub>3</sub> can be controlled by the MOF preparation method. Furthermore, these materials exhibited exceptionally high performance in catalyzing the oxidation of volatile organic compound (VOC).

## Experimental

### Materials

All reagents were commercially available and used as received without further purification. Analytical-grade Cr(NO<sub>3</sub>)<sub>3</sub>·9H<sub>2</sub>O (>99%), terephthalic acid (>99%) and *N,N*-dimethylformamide (DMF) (>98%) were purchased from J&K Scientific Ltd. Cr<sub>2</sub>O<sub>3</sub> powder (>99%) was purchased from Thermo Fisher Scientific

Center for Aircraft Fire and Emergency, Civil Aviation University of China, Tianjin 300300, China. E-mail: zhouxm@nankai.edu.cn

† Electronic supplementary information (ESI) available: Supplementary figures and tables. See DOI: 10.1039/c9ra00206e



Ltd. Hydrofluoric acid (40%) and formaldehyde solution (38%) was obtained from Beijing Chemical Co., Ltd. (Beijing, China).

### Preparation of MOFs: MIL-88B(Cr) and MIL-101(Cr)

MIL-88B(Cr) and MIL-101(Cr) were synthesized according to the previous reports after a minor modification.<sup>24,25</sup> Typically, for the synthesis of MIL-88B(Cr), the mixture of  $\text{Cr}(\text{NO}_3)_3 \cdot 9\text{H}_2\text{O}$  (1.6 g, 4 mmol), terephthalic acid (0.66 g, 4 mmol), hydrofluoric acid (12 mmol) and DMF (30 mL) was placed in a 50 mL Teflon autoclave and then heated at 210 °C for 24 h. After natural cooling, the mixture was collected by centrifugation. The resulting powder was ultrasonically washed with DMF and ethanol, respectively. The final product of MIL-88B(Cr) was obtained by dried in a vacuum oven (80 °C) for 8 h. For the synthesis of MIL-101(Cr), the mixture of  $\text{Cr}(\text{NO}_3)_3 \cdot 9\text{H}_2\text{O}$  (2 g, 5 mmol), terephthalic acid (0.83 g, 5 mmol), hydrofluoric acid (5 mmol) and  $\text{H}_2\text{O}$  (30 mL) was placed in a 50 mL Teflon autoclave and then heated at 220 °C for 8 h. After natural cooling, the mixture was collected by centrifugation. The resulting powder was ultrasonically washed with DMF and ethanol, respectively. The final product of MIL-101(Cr) was obtained by dried in a vacuum oven (80 °C) for 8 h.

### Preparation of 3D mesoporous $\text{Cr}_2\text{O}_3$ : AC-88B and AC-101

The carbonization of MIL-88B(Cr) and MIL-101(Cr) was carried out in a tube furnace at 600 °C for 5 h under  $\text{N}_2$  gas atmosphere with a heating rate of 5 °C  $\text{min}^{-1}$ . After carbonization, the samples were cooled to room temperature under  $\text{N}_2$  flow. Then, the auto-combustion of the resulting samples occurred when there were taken out of the tube furnace and exposed to air. After full combustion, the final products of 3D mesoporous  $\text{Cr}_2\text{O}_3$ : AC-88B and AC-101 were obtained.

To make a comparison, MIL-101(Cr) was also carbonized at 750 °C and 900 °C, respectively, for 5 h under  $\text{N}_2$  gas atmosphere. And the resulting samples were exposed to air after carbonization. Additionally, the unburned sample of MIL-101(Cr) carbonized at 600 °C was prepared by deactivation method with introducing nitrogen-oxygen atmosphere (2%  $\text{O}_2$  by volume) before expose to air.

### Characterizations

The adsorption-desorption isotherm of nitrogen was measured by Micromeritics ASAP 2460 automated gas sorption system at -196 °C, after the sample was degassed under vacuum at 300 °C for 4 h. The specific surface areas of all samples were calculated by the BET method, and the average pore diameters were determined by Barret-Joyner-Halenda (BJH) method.

Thermal gravimetric analysis (TGA) was performed on TGA/SDT851 (Mettler-toledo, CH) with heating rate of 10 °C  $\text{min}^{-1}$  in air flow.

The XRD patterns of the samples were recorded on a Rigaku D/max-2500 power diffractometer using  $\text{Cu K}\alpha$  radiation (40 kV and 100 mA) in the  $2\theta$  range from 10° to 80° with a scan rate of 0.3°  $\text{min}^{-1}$ .

SEM analyses were performed (JEOL, Model JSM-7500F) at an acceleration voltage of 10 kV. TEM images were acquired on

a FEI Tecnai G2 F20 operating at 200 keV. Diffraction patterns were recorded on a Gatan UltraScan 1000XP CCD camera. TEM samples were prepared by drop-casting 100  $\mu\text{L}$  of sample suspension (ground sample powder dispersed in ethanol) on carbon grids. XPS measurements were acquired on a Kratos Axis Ultra DLD multitechnique X-ray photoelectron spectrometer (UK) equipped with a monochromatic  $\text{Al K}\alpha$  X-ray source ( $h\nu = 1486.6$  eV). All XP spectra were recorded using an aperture slot measuring 300  $\mu\text{m} \times 700 \mu\text{m}$ . Survey and high-resolution spectra were recorded with pass energies (within  $\pm 0.2$  eV) were determined, with respect to the position of the adventitious C 1s peak at 284.6 eV.

### Catalytic evaluation

The catalytic performance test was evaluated in a continuous flow fixed-bed quartz reactor (i.d. = 6 mm). 200 mg of the catalyst (40–60 mesh) was loaded together with silicon dioxide powder (40–60 mesh) to dilute the sample and avoid temperature gradients. The feed gas was 600 ppm formaldehyde balanced with the air, which was obtained by passing an air flow through a 38 wt%  $\text{HCHO}$  solution at 0 °C. The space velocity (SV) was 90 000  $\text{mL (g h)}^{-1}$ . The outlet mixture was analyzed on-line by a Shimadzu GC-2010 plus gas chromatograph equipped with a GDX-403 packed column and TCD detector.

## Results and discussion

3D porous  $\text{Cr}_2\text{O}_3$  with bipyramidal hexagonal prismatic and octahedral morphology were derived from MIL-88B(Cr) and MIL-101(Cr), respectively, *via* auto-combusting in air after carbonization under  $\text{N}_2$ . And the corresponding  $\text{Cr}_2\text{O}_3$  samples were denoted as AC-88B and AC-101, respectively. The X-ray diffraction (XRD) patterns of AC-88B and AC-101 present diffraction peaks characteristic of a  $\text{Cr}_2\text{O}_3$  phase (PDF# 38-1479) without any impurities (Fig. 1). Scanning electron microscopy (SEM) analysis indicates that AC-88B exhibited bipyramidal hexagonal prismatic mesoporous structures with sizes of 1.0–

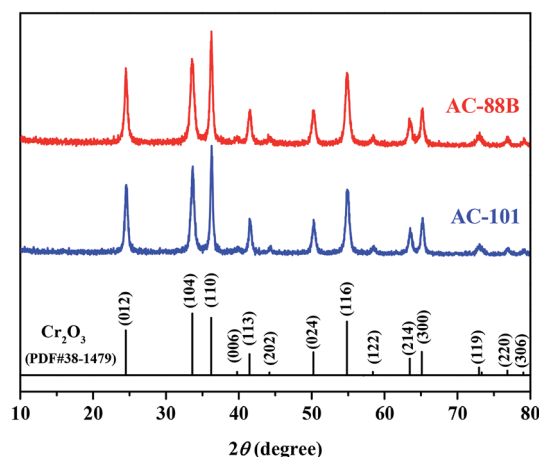


Fig. 1 XRD patterns of AC-88B and AC-101. Standard reference peaks of  $\text{Cr}_2\text{O}_3$  was also included.



1.5  $\mu\text{m}$  in length and 200–300 nm in width (Fig. 2b) and AC-101 exhibited octahedral mesoporous structures with sizes of 200–400 nm (Fig. 2f). The morphology of AC-88B and AC-101 were well consistent with their MOF templates of MIL-88B(Cr) (Fig. 2a) and MIL-101(Cr) (Fig. 2e), respectively. From the transmission electron microscopy (TEM) images (Fig. 2c and g), we can see that the two 3D structures were both composed of clustered  $\text{Cr}_2\text{O}_3$  nanoparticles with size of <30 nm. The high-resolution TEM (HRTEM) images of AC-88B and AC-101 show lattice fringes with interplanar of *ca.* 0.36 nm, corresponding to the (012) plane of  $\text{Cr}_2\text{O}_3$  phase (Fig. 2d and h). This further confirms the results of XRD analysis. What's more, in addition to the good shape control, the size of 3D mesoporous  $\text{Cr}_2\text{O}_3$  can also be regulated by controlling the synthesis conditions of their MOF templates.<sup>26–30</sup> For example, *ca.* 800 nm octahedral mesoporous  $\text{Cr}_2\text{O}_3$  were fabricated from *ca.* 900 nm MIL-101(Cr) *via* lowering the concentration of reactants and extending the reaction time (Fig. S1†). As compared to MIL-101(Cr), the size of corresponding porous  $\text{Cr}_2\text{O}_3$  decreased a little, which was resulted from the decomposition and contraction when being heated.

The X-ray photoelectron spectroscopy (XPS) analysis was carried out to further investigate the oxidation state of chromium. From Fig. 3a and b, one can see Cr 2p<sub>3/2</sub> peak of AC-88B and AC-101 that could be resolved into the three components at BE = *ca.* 578.2, 576.4 and 575.2 eV, ascribable to  $\text{Cr}^{5+}$ ,  $\text{Cr}^{3+}$  and  $\text{Cr}^{2+}$ , respectively.<sup>10,31</sup> The results of quantitative analyses on the Cr 2p<sub>3/2</sub> spectra were summarized in Table S1.† Apparently, the surface  $\text{Cr}^{3+}$  species on both of AC-88B and AC-101 were the highest content; in addition, the surface  $\text{Cr}^{5+}$  contents on both of AC-88B and AC-101 were higher than 11%. It has been proved that the co-presence of multivalent chromium atoms was beneficial for the improvement in activity of the catalyst.<sup>10,11</sup>

The nitrogen sorption results of AC-88B and AC-101 (Fig. 3c and d) suggest the existence of different pore sizes spanning from meso- to macropores. The slight hysteresis of the desorption curves at medium relative pressure demonstrate the existence of mesopores, while the final almost vertical tail at high relative pressure ( $p/p_0 > 0.9$ ) reveal the presence of macropores. Furthermore, the hysteresis loops at  $p/p_0 > 0.8$  in the adsorption/desorption isotherms indicate the condensation of nitrogen in the irregular pores between the particles, *i.e.*

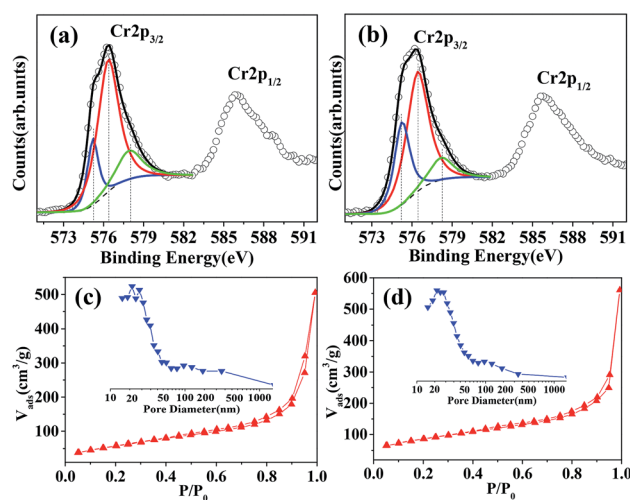


Fig. 3 XPS core level spectra of Cr 2p for (a) AC-88B and (b) AC-101.  $\text{N}_2$  sorption isotherms and the corresponding pore distribution (inset) of (c) AC-88B and (d) AC-101.

intergranular porosity.<sup>32</sup> The pore size distribution curves of AC-88B and AC-101 (inset of Fig. 3c and d) show that the mesopore sizes were centered at *ca.* 20 nm, while the macropore sizes were ranged from 50 to 200 nm. The specific surface areas of AC-88B and AC-101 were calculated to be 219.25  $\text{m}^2 \text{g}^{-1}$  and 303.44  $\text{m}^2 \text{g}^{-1}$ , respectively. As we know, this is the highest specific surface area of the reported porous  $\text{Cr}_2\text{O}_3$  so far.

The results of thermogravimetric analysis (TGA) (Fig. S2†) show that there is only one slight weight loss peak for both of AC-88B and AC-101 at 200–300  $^\circ\text{C}$ , corresponding to the loss of residual carbon. But the carbon content is very low (*ca.* 1.2%), which can be neglected to the specific surface areas of AC-88B and AC-101.

It should be noted that the auto-combustion phenomenon of carbonized Cr-MOF (Fig. S3†) only occurred at a relative low carbonization temperature (normally, lower than 700  $^\circ\text{C}$ ). To study the mechanism of auto-combustion, the samples of MIL-101(Cr) carbonized at 600  $^\circ\text{C}$ , 750  $^\circ\text{C}$  and 900  $^\circ\text{C}$  were prepared, respectively. To avoid auto-combustion, the sample carbonized at 600  $^\circ\text{C}$  was deactivated with nitrogen–oxygen atmosphere (2%  $\text{O}_2$  by volume). From their TEM and HRTEM images (Fig. S4†), it clearly shows that the size and the crystallinity of

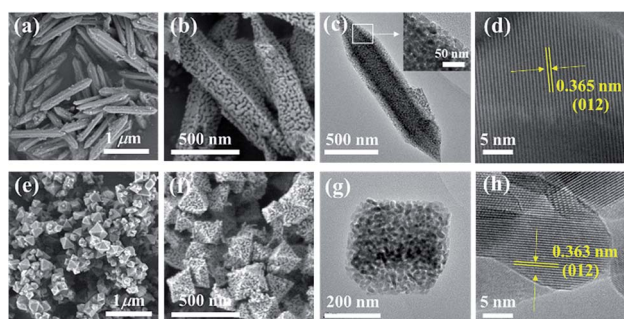


Fig. 2 SEM images of (a) MIL-88B(Cr) and (b) AC-88B. (c) TEM image and (d) HRTEM image of AC-88B. SEM images of (e) MIL-101(Cr) and (f) AC-101. (g) TEM image and (h) HRTEM image of AC-101.

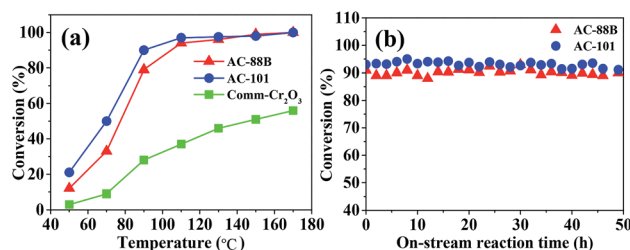


Fig. 4 (a) Conversion of formaldehyde over AC-88B and AC-101 at different reaction temperatures. (b) Stability of AC-88B and AC-101 for the oxidation of formaldehyde at 100  $^\circ\text{C}$  under the conditions of  $\text{HCHO} = 600 \text{ ppm}$  and  $\text{SV} = 90\,000 \text{ mL (g h)}^{-1}$ .





chromium oxide nanoparticles increased with the temperature increasing, which was consistent with the XRD results (Fig. S5†). XPS analysis reveals that  $\text{Cr}^{3+}$  species was the only content on the surface of samples carbonized at 750 °C and 900 °C, while  $\text{Cr}^{2+}$  species was detected when the carbonization temperature decreased to 600 °C. In the fact, there will be more low valent chromium in the original sample than the deactivated ones, since some of the low valent chromium would transform to  $\text{Cr}^{3+}$  in the process of deactivation. Thus, the reason of auto-combustion for Cr-MOFs carbonized at low temperature should be due to the presence of nanosized low valent chromium with high surface activity, while the high temperature carbonized samples would not auto-combust for the formation of stable and large  $\text{Cr}_2\text{O}_3$  particles. Moreover, these high temperature carbonized Cr-MOFs would not convert to 3D porous  $\text{Cr}_2\text{O}_3$  with controlled shape and high specific surface area, even they are further calcinated in air, as seen in Fig. S7 and S8† (the structure of the resulting  $\text{Cr}_2\text{O}_3$  samples were collapsed after calcinated in air and the corresponding specific surface area was lower to  $47.11 \text{ m}^2 \text{ g}^{-1}$ ).

The catalytic performances of AC-88B and AC-101 were examined by the complete oxidation of formaldehyde (a major VOC pollutant to the environment). The experiment results (Fig. 4a) indicate that the formaldehyde conversion increased with the rise of reaction temperature. For both of AC-88B and AC-101, the formaldehyde conversions improved remarkably from 50 °C to 90 °C and reached to 90% at 100 °C and 90 °C, respectively, even at a high space velocity (SV), which was much superior in catalytic performance to the ordered mesoporous  $\text{Cr}_2\text{O}_3$  prepared with KIT-6 as hard template.<sup>10</sup> More importantly, compared to the commercial  $\text{Cr}_2\text{O}_3$  (comm- $\text{Cr}_2\text{O}_3$ ), the 3D mesoporous  $\text{Cr}_2\text{O}_3$  prepared in this work exhibited exceptionally high performance which may be benefited from the high specific surface area and the concomitant multivalent chromium atoms of the catalysts (the commercial  $\text{Cr}_2\text{O}_3$  only have  $\text{Cr}^{3+}$  and its specific surface area is  $0.66 \text{ m}^2 \text{ g}^{-1}$ , as shown in Fig. S9 and S10,† respectively).<sup>11,12</sup> The stabilities of AC-88B and AC-101 were also tested within 50 hours of on-stream reaction (Fig. 4b). Apparently, the conversions were quite stable with time on-stream, indicating the high stability of AC-88B and AC-101. In fact, these catalysts could be recovered efficiently by a simple catalytic combustion procedure to remove organic pollutants because of their stability at high temperatures.

## Conclusions

In summary, we provide a novel method to synthesize 3D porous  $\text{Cr}_2\text{O}_3$  with high specific surface area (up to  $303.44 \text{ cm}^2 \text{ g}^{-1}$ ) via MOF auto-combustion. More importantly, the shape and size of the 3D mesoporous  $\text{Cr}_2\text{O}_3$  can be good controlled by a facile adjustment of MOF synthesis conditions. Furthermore, benefiting from the porous structural property and the co-presence of multivalent chromium, these materials showed an exceptionally high catalytic performance in formaldehyde oxidation. These results provide a novel method in designing and synthesis of various shapes and sizes 3D porous  $\text{Cr}_2\text{O}_3$ . The

potential applications of these 3D porous  $\text{Cr}_2\text{O}_3$  as other catalysts, adsorbents, gas sensors, electrodes and electromagnetics will be studied in our next research.

## Conflicts of interest

There are no conflicts to declare.

## Acknowledgements

This work was supported by the National Natural Science Foundation of China (No. 51776219) and the Fundamental Research Funds for the Central Universities (No. 3122018C026).

## Notes and references

- H. Du, X. Guo, R.-M. Kong and F. Qu, *Chem. Commun.*, 2018, **54**, 12848–12851.
- A. C. Santulli, M. Feyngenson, F. E. Camino, M. C. Aronson and S. S. Wong, *Chem. Mater.*, 2011, **23**, 1000–1008.
- H. Sun, L. Wang, D. Chu, Z. Ma and A. Wang, *Mater. Lett.*, 2015, **140**, 35–38.
- B. Bo, P. Wang, W. Le, Y. Li and Z. Chen, *Mater. Chem. Phys.*, 2009, **114**, 26–29.
- Y. K. Bai, R. T. Zheng, Q. Gu, J. J. Wang, B. S. Wang, G. A. Cheng and G. Chen, *J. Mater. Chem. A*, 2014, **2**, 12770–12775.
- L. Chen, Z. Song, X. Wang, S. V. Prikhodko, J. Hu, S. Kodambaka and R. Richards, *ACS Appl. Mater. Interfaces*, 2009, **1**, 1931–1937.
- L. Hao, D. Xiwen, X. Xianran, W. Guoxiu and Q. Shi Zhang, *Chem. Commun.*, 2012, **48**, 865–867.
- H. Ma, Y. Xu, Z. Rong, X. Cheng, S. Gao, X. Zhang, H. Zhao and L. Huo, *Sens. Actuators, B*, 2012, **174**, 325–331.
- K. Jiao, B. Zhang, B. Yue, Y. Ren and S. Liu, *Chem. Commun.*, 2005, **45**, 5618.
- Y. Xia, H. Dai, L. Zhang, J. Deng, H. He and C. T. Au, *Appl. Catal., B*, 2010, **100**, 229–237.
- A. K. Sinha and S. Kenichirou, *Angew. Chem.*, 2004, **117**, 275–277.
- A. K. Sinha and K. Suzuki, *Appl. Catal., B*, 2007, **70**, 417–422.
- X. Yu, S. Yan and K. Chen, *Appl. Surf. Sci.*, 2018, **439**, 298–304.
- L. Qiao, Z. Fu, J. Li, J. Ghosen, M. Zeng, J. Stebbins, P. N. Prasad and M. T. Swihart, *ACS Nano*, 2017, **11**, 6370–6381.
- S. Ni, X. Wang, G. Zhou, F. Yang, J. Wang, Q. Wang and D. He, *J. Alloys Compd.*, 2010, **505**, 727–732.
- X. Mou, X. Wei, L. Yong and W. Shen, *CrystEngComm*, 2012, **14**, 5107–5120.
- L. Zong, J. Zhao and J. Zhang, *Chem. Eng. J.*, 2018, **343**, 500–511.
- M. Wang, J. Ioccozia, L. Sun, C. Lin and Z. Lin, *Energy Environ. Sci.*, 2017, **7**, 2182–2202.
- X. Xu, R. Cao, S. Jeong and J. Cho, *Nano Lett.*, 2012, **12**, 4988–4991.



- 20 J. Shao, Z. Wan, H. Liu, H. Zheng, T. Gao, M. Shen, Q. Qu and H. Zheng, *J. Mater. Chem. A*, 2014, **2**, 12194–12200.
- 21 X. J. Zhang, W. Qin, D. S. Li, D. Yan, B. W. Hu, Z. Sun and L. K. Pan, *Chem. Commun.*, 2015, **51**, 16413–16416.
- 22 G. C. Li, P. F. Liu, R. Liu, M. Liu, K. Tao, S. R. Zhu, M. K. Wu, F. Y. Yi and L. Han, *Dalton Trans.*, 2016, **45**, 13311–13316.
- 23 A. A. Voskanyan, C. Y. V. Li, K. Y. Chan and L. Gao, *CrystEngComm*, 2015, **17**, 2620–2623.
- 24 Y. H. Shih, S. H. Lo, N. S. Yang, B. Singco, Y. J. Cheng, C. Y. Wu, I. H. Chang, H. Y. Huang and C. H. Lin, *Chempluschem*, 2012, **77**, 982–986.
- 25 G. Férey, C. Mellot-Draznieks, C. Serre, F. Millange, J. Dutour, S. Surblé and I. Margiolaki, *Science*, 2005, **309**, 2040–2042.
- 26 V. I. Isaeva, A. L. Tarasov, V. V. Chernyshev and L. M. Kustov, *Mendeleev Commun.*, 2015, **25**, 466–467.
- 27 D. Jiang, A. D. Burrows and K. J. Edler, *CrystEngComm*, 2011, **13**, 6916–6919.
- 28 F. Tan, L. Min, K. Li, Y. Wang, J. Wang, X. Guo, G. Zhang and C. Song, *Chem. Eng. J.*, 2015, **281**, 360–367.
- 29 P. Sarawade, H. Tan, D. Anjum, D. Cha and V. Polshettiwar, *Chemsuschem*, 2014, **7**, 529–535.
- 30 J. Campbell and B. Tokay, *Microporous Mesoporous Mater.*, 2017, 251.
- 31 R. Nowak, P. Hess, H. Oetzmänn and C. Schmidt, *Appl. Surf. Sci.*, 1989, **43**, 11–16.
- 32 W. Hui, Z. Ying, L. Zhang, Y. Guo, S. Liu, G. Fei, H. Yang, G. Feng, L. Xue and G. Lei, *RSC Adv.*, 2016, **6**, 84871–84881.

